Electromigration in transition metals. II. Light interstitials in Cu, Ag, Ni, Pd, Al, V, Nb and Ta



1991 J. Phys.: Condens. Matter 3 7331

(http://iopscience.iop.org/0953-8984/3/38/008)

J. Phys.: Condens. Matter 3 (1991) 7331–7361. Printed in the UK

# Electromigration in transition metals: II. Light interstitials in Cu, Ag, Ni, Pd, Al, V, Nb and Ta

J van Ek and A Lodder
Faculteit der Natuurkunde en Sterrenkunde, Vrije Universiteit, De Boelelaan 1081, 1081 HV Amsterdam, The Netherlands

Received 4 December 1990

**Abstract.** The electromigration wind valence of interstitial hydrogen in a series of transition metals is calculated using a state-of-the-art computational scheme accounting for the real band structure and local lattice deformation plus charge transfer in the impurity cluster. A microscopic picture of the oscillatory motion and the mobility of the proton explains the remarkable difference between the wind valence of hydrogen in Nb and Ta. A zero-point motion model explains the H/D isotope effect in the effective valence as observed in many systems. From a comparison of experimental effective valences with calculated wind valences, it is concluded that the direct valence, in systems where the wind valence is not dominant, has a value close to unity. Thermal effects are investigated and shown to be unimportant at moderate temperatures. In addition wind valences of interstitial boron in Pd, carbon in Pd and Nb and oxygen in Nb are presented.

## 1. Introduction

Until the end of the 1970s there was a vast interest in metal/hydrogen systems. On the one hand, these systems seemed to offer applications in energy storage with hydrogen as the energy carrier. On the other hand, hydrogen embrittlement of initially ductile metals was an important topic in materials technology. Along with these technological issues more fundamental properties of metal/hydrogen systems have been investigated too. Besides measurements on the de Haas–van Alphen (dHvA) effect and residual resistivity at low hydrogen concentrations in nearly perfect metallic hosts, changes in electronic structure and superconducting properties at higher concentrations have been investigated. For most properties (except for the residual resistivity) a clear H/D isotope effect was observed. Using various methods of structure determination (x-ray and neutron diffraction, transmission electron microscopy) the complex phase diagrams of many metal/hydrogen systems could be determined. Hydrogen in binary alloys is used as a local probe, sampling the composition of its direct surroundings [1].

Owing to its relatively high mobility in most metals, even at room temperature, transport of hydrogen due to a concentration, temperature, stress and electric potential gradient, and combinations of these forces, is readily observed in many metals. In the latter case an electric field interacts with a distribution of hydrogen atoms dissolved in the host metal. The large mobility causes a hydrogen concentration gradient to be built up within a reasonable time span at moderate temperatures. The direction of this gradient in the steady state [2] depends in the effective valence $Z^*$ of the hydrogen atom

0953-8984/91/387331 + 31 $03.50  

in the metal under consideration. Also in this quantity a H/D isotope effect has been observed.

The effective valence is commonly viewed as being composed of two parts. First, the electric field interacts with the impurity nucleus and with the screening electrons surrounding it while the nucleus and the electrons in turn have an attractive interaction. The net susceptibility to the field is expressed by the direct valence, $Z_{\text{direct}}$. Secondly, the non-equilibrium distribution for the conduction electrons in the current-carrying metal will lead to a non-symmetric charge distribution around the hydrogen atom. This effect is proportional to the current density, and in many cases (but not all!) a force is exerted on the hydrogen atom in the direction of the net electron flow. Naively this can be pictured as the result of an electron wind blowing against the hydrogen, giving rise to the so-called wind valence, $Z_{\text{wind}}$. The signs and relative magnitudes of these two contributions determine whether impurity transport takes place towards the cathode or the anode in an experimental set-up.

Measured effective valences of hydrogen in metals exhibit many features which are not fully understood yet. There is the very different behaviour of $Z^*$ as a function of temperature in V and Nb versus Ta, although the electronic structures of these transition metals are commonly regarded as being very similar. A H/D isotope effect for which $|Z_{\text{D}}^*| > |Z_{\text{H}}^*|$ was observed in V, Fe, Ni and Ag whereas in Pd, Nb and Ta the reverse behaviour was found [3]. Further, until now, experiments have not been able to determine unambiguously the value of the direct valence of hydrogen in pure metals. Carefully designed experiments on $Nb_xV_{1-x}(H)$ strongly suggest that it might be close to the value of +1 [4].

Additionally one needs a link between calculated quantities and the effective valence $Z^*$, which was introduced as a phenomenological parameter for analysing electromigration experiments [5]. The scalar character of the effective valence is not so obvious when adopting a microscopic point of view for any impurity in a metal. In general the calculated effective valence will be a position-dependent tensor, which must be reduced to a scalar in order to be able to make a comparison with experiment.

In this paper the phenomenon of electromigration of small interstitials such as H, B, C, N and O in various metals will be modelled as follows. The perfect crystal structure is assumed for the host metal, while in the dilute limit it suffices to consider one single impurity plus its perturbed surroundings, for the interstitials do not interact. The wind valence is calculated according to a Korringa–Kohn–Rostoker (KKR) Green function description of this embedded impurity cluster, which is treated in the preceding paper [6] (hereafter referred to as I). Because the wind valence results only from the interaction of the impurity with electrons at the Fermi energy ($T = 0$) or just around the Fermi energy ($T \neq 0$), it is far more accessible through a theoretical/computational treatment than the direct valence. The latter can be regarded as being the result of self-consistent screening of the impurity *at all energies* and the interaction of the electric field with this screened entity.

In section 2 experimental data on the systems under consideration will be compiled. These effective valence values will be discussed with regard to possible experimental difficulties and their dependence on temperature and concentration of the interstitial.

The first subsection of section 3 describes the reduction of the calculated local wind valence tensor to a scalar quantity. Further the procedure for obtaining a temperature-dependent value for the transport relaxation time introduced in I will be elucidated. The next subsection discusses the construction and the quality of the potentials used. The migrating entity, previously addressed in I, will be defined as well as the adopted migration paths.

Results on the wind valence of interstitials in Cu, Ag, Ni, Pd, Al, V, Nb and Ta will be presented in section 4. The basic nature of the wind valence will be investigated. An explanation for the observed H/D isotope effect is offered. The last subsection deals with a possible temperature effect caused by the fact that at experimental temperatures the Fermi–Dirac distribution function will not have a sharp cut-off at the Fermi energy.

Applicability of the results to the fundamental question of the magnitude of the direct valence in real metals is discussed in section 5. Conclusions based on the present work are gathered.

## 2. Experimental data

In table 1 available experimental data on various metal/hydrogen systems are summarized. These results have been obtained using different experimental techniques at different hydrogen concentrations in polycrystalline metal samples. In the coinage metals Ni, Cu [7] and Ag [8] the solubility of hydrogen is very low, which might give rise to experimental difficulties, especially in polycrystalline samples. In addition the results on Ag(H/D) and Ni(H/D) have been seriously questioned in that they might be a factor of 2 too low due to a systematic experimental error [9].

Over a period of years Marêché, Rat and Hérold [10, 11] have been investigating the effective valence of the two hydrogen isotopes in $\alpha$-Pd(H/D) using different techniques. In their most recent paper they achieved the lowest impurity concentration. The resulting values for $Z^*$ are quoted in table 1. The agreement between the different values for the effective valence of hydrogen in palladium reported in the literature over a period of some 35 years is gratifying. For temperatures ranging from 420 to 1070 K at concentrations less than $4 \times 10^{-2}$ all effective valences are found above $+0.3$ but below $+0.7$, for both H and D.

Like in Pd the solubility of hydrogen is also large in the BCC transition metals V, Nb and Ta. As a consequence the amount of experimental data is relatively large too. The effective valences in table 1 were taken from a paper by Erckmann and Wipf [12] in which they investigated the temperature dependence of $Z^*$ at different hydrogen and deuterium concentrations in V, Nb and Ta by means of steady-state resistance measurements. The linear extrapolation to zero concentration at $T = 375$ K gave a positive effective valence in all three cases. In the case of V at $T = 375$ K the extrapolation agrees within 10% with the results of Pine and Cotts [13] for H and D and of Nakajima *et al* [14] for H. More recently Verbruggen *et al* [2] used a capacitive multidilatometer to obtain accurate results on V(H), Nb(H) and Ta(H) as a function of temperature with $c_H \simeq 0.01$. The qualitative agreement between the outcome of various experiments confirms the different behaviour of $Z^*(T)$ for V(H) and Nb(H), where $\partial Z^*/\partial T < 0$, versus Ta(H), having a positive slope.

Concentration differences, and differences in sample preparation and in experimental techniques mean that no direct comparison is possible and that the values for $Z^*$ quoted in table 1 must be handled with care. Nevertheless reality can be attributed to the existence of a H/D isotope effect because this comes from experiments performed under identical conditions.

Apart from hydrogen or deuterium, effective valences of C, N and O in vanadium [15], C and O in niobium [16, 17] and C and O in tantalum [16, 18] have been measured. These experiments had to be carried out at very high temperatures in order to enhance the mobility of the interstitials, which are present in low concentrations ($c < 0.006$). In

**Table 1.** Effective valences $Z^*$ of hydrogen and deuterium as measured in various metals at temperature $T$. The atomic fraction of hydrogen or deuterium $c$, the Hall coefficient $R_H$ at 293 K and references are given in the last three columns. For the BCC metals effective valences obtained from an extrapolation to $c = 0$ are given.

| | System | $Z_H^*$ | $Z_D^*$ | $T$ (K) | $c$ | $R_H$ ($10^{-11}$ m$^3$ A$^{-1}$ s$^{-1}$) | Ref. |
|---|---|---|---|---|---|---|---|
| FCC | Cu(H) | −15 to −20 | — | 1170–1270 | — | −5.2 | [51] |
| | Ag(H) | −6.8 | −18 | 750–980 | $\leqslant 1.8 \times 10^{-6}$ | −8.8 | [8] |
| | Ni(H) | +0.67 to +0.57 | +0.84 to +0.74 | 720–920 | $\leqslant 3.0 \times 10^{-4}$ | −6.0 | [3] |
| | Pd(H) | +0.44 | +0.35 | 970 | $\leqslant 8.2 \times 10^{-3}$ | −7.6 | [11] |
| BCC | V(H) | +1.7 | +1.9 | 375 | 0 | 8.0 | [12] |
| | Nb(H) | +2.7 | +2.4 | 375 | 0 | 8.8 | [12] |
| | Ta(H) | +0.5 | +0.4 | 375 | 0 | 10 | [12] |

all cases a positive sign of $Z^*$ was found, except for the case of Nb(O) where a change of sign at $T = 2100$ K ($\partial Z^*/\partial T < 0$) was observed. There seems to be no strong temperature dependence in V (1900 K $< T <$ 2100 K), which leads to average values of 2.2, 1.6 and 1.2 for C, N and O respectively. For C in Nb and Ta appropriate average values for $Z^*$ around 2400 K are 2.6 and 3.2 respectively. Only for Nb(O) and Ta(O) was a strong temperature dependence reported in the range from 1500 K to 2400 K.

The last but one column in table 1 displays the Hall coefficient of the pure host metals at room temperature. Sometimes the sign of the wind valence is linked with the sign of the Hall coefficient, thus introducing the rather curious picture of electrons and holes in a metal being scattered by an impurity. In those terms a positive Hall coefficient would imply dominant hole scattering due to the presence of a hole band. A positive wind valence would be the result. Such considerations, however, deny the fact that in a metal a description in terms of occupied (electron) states or in terms of unoccupied (hole) states is equivalent [19].

In addition to the transition-metal systems mentioned above Al(H) will be investigated, aluminium being a simple trivalent FCC metal. No data on $Z^*$ are known, presumably due to the extremely low solubility of hydrogen in aluminium [20]. There exists some interest in the wind valence on $\mu^+$ and H in the context of light-particle tunnelling in metals [21, 22].

## 3. Calculation of the wind valence

The main purpose of the present paper is to compare calculated wind valences $Z_{\text{wind}}$ with experimental effective valences $Z^*$. A calculation of the wind valence based on the method as described in I, however, leads to a position-dependent $3 \times 3$ wind valence tensor $\underline{Z}_{\text{wind}}(\boldsymbol{R}_l)$ divided by the average transport relaxation time $\tau$. In this section some crucial ideas behind the model and ingredients of the model are discussed.

Subsection 3.1 treats the reduction of $\underline{Z}_{\text{wind}}(\boldsymbol{R}_l)$ to $Z_{\text{wind}}$. The construction of the potentials that describe the host metal and the impurity cluster are discussed in subsection 3.2. In subsection 3.3 the procedure used to obtain the transport relaxation time is discussed. Finally, in subsection 3.4, the choice of vital parameters in the impurity cluster, such as the size of the migrating entity, the migration paths and the lattice deformation induced by the interstitial, is motivated.

### *3.1. Scalar wind valence*

Imagine an interstitial impurity oscillating around its equilibrium position in a metal lattice amidst its perturbed surroundings. The probability density for the impurity is denoted by $P(\boldsymbol{R}_l)$ and has a pronounced peak at the equilibrium position $\boldsymbol{R}_l = 0$. The surrounding host atoms are taken at rigid positions shifted slightly from the original lattice sites in a radial outward direction. This means that the metal atoms are unable to follow the extremely rapid oscillations of the interstitial instantaneously. This relaxation of the surrounding atoms to slightly shifted positions is responsible for the self-trapping of interstitial impurities [23, 24]. Localized states described by $P(\boldsymbol{R}_l)$ are appropriate rather than delocalized band states for interstitials moving over a periodic lattice of impurity sites.

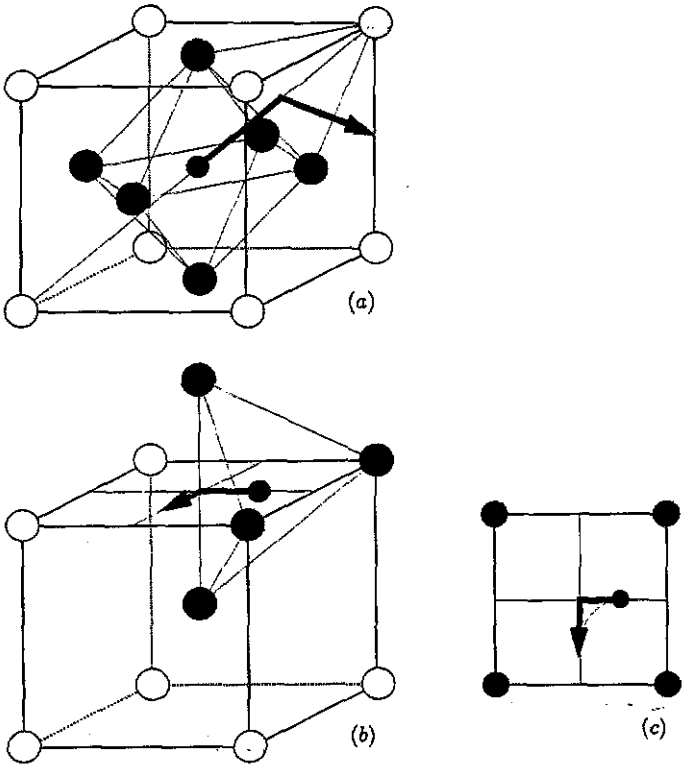


**Figure 1.** (*a*) FCC unit cell with migration path starting in the [1 1 1] direction from the octahedral towards the tetrahedral site. (*b*) BCC unit cell with migration path from tetrahedral site towards octahedral site along [1 0 0] direction. (*c*) Top view of (*b*) showing how the curved path is approximated by paths in the [1 0 0] directions.

An elementary step in the diffusive motion of an interstitial impurity in a lattice gas will be assumed to proceed via a classical over-barrier jump mechanism. Presumably quantum mechanical tunnelling processes come into play at low temperatures in BCC metals. Such a mechanism for light particle diffusion will be virtually absent in FCC metals due to the much larger distance between two neighbouring sites.

Classical diffusion of the interstitial impurity to a neighburing site is assumed to take place along directions in which $P(\boldsymbol{R}_l)$ still is appreciable. This is reasonable since, for an impurity oscillating in its ground state, low energy regions of the potential energy surface for the interstitial do give rise to appreciable values of $P(\boldsymbol{R}_l)$. Classical trajectories over the potential energy surface are at the heart of such a low energy region or connect two such regions separated by a potential barrier. As an example a hydrogen atom at an octahedral site in Pd, being an FCC metal, is considered. One immediately supposes that $P(\boldsymbol{R}_l)$ will be more extended in the [1 1 1] direction than in the [1 0 0] direction (see figure 1(*a*)). Towards the surrounding atoms in the [1 0 0] directions $P(\boldsymbol{R}_l)$ will vanish even more rapidly. Actual effective-medium calculations of $P(\boldsymbol{R}_l)$ in Pd(H) at a lattice distortion of $0.008a$, $a$ being the lattice constant, confirm this supposition [23]. Thus the mobility of an interstitial is tightly connected to $P(\boldsymbol{R}_l)$ but when an interstitial impurity actually jumps to a neighbouring site the picture of rigidly positioned metal atoms collapses. However a diffusion jump takes place approximately every $10^{-11}$–$10^{-12}$ s [25] while a hydrogen atom oscillates with a frequency of order $10^{13}$ Hz. Therefore quantum

mechanical averaging of $\boldsymbol{R}_I$-dependent quantities over $\boldsymbol{R}_I$ weighted by $P(\boldsymbol{R}_I)$ can be considered as justified.

When an electric field $\boldsymbol{E}$ is present the impurity will experience a force $\boldsymbol{F}(\boldsymbol{R}_I)$ that is assumed to be linear in the field

$$\boldsymbol{F}(\boldsymbol{R}_I) = \underline{Z}^*(\boldsymbol{R}_I)e\boldsymbol{E}. \tag{1}$$

The rank-2 tensor $\underline{Z}^*(\boldsymbol{R}_I)$ is the microscopic analogue of the effective valence $Z^*$. The reduction of $\underline{Z}^*(\boldsymbol{R}_I)$ to $Z^*$ is based on the insight that any result from an electromigration experiment is due to only those impurity atoms that have been able to diffuse through the sample. In order to determine $Z^*$ the impurities must, apart from being susceptible to the electric field, be mobile too. Imagine, for example, a substitutional impurity in an otherwise perfect metal lattice. An electric field is present. There will almost certainly be a wind force on the impurity because of conduction electron scattering, but owing to its immobility (no vacancies present) it is impossible, in practice, to measure its effective valence although different from zero. So what really matters on a microscopic scale is the component of the driving force in the direction along which the impurity is mobile. These directions will coincide with migration paths in classical diffusion and thus with regions in space where $P(\boldsymbol{R}_I)$ has an appreciable value.

Upon introduction of a coordinate

$$s \equiv s(\boldsymbol{R}_I) \tag{2}$$

along a migration path with tangent unit vectors

$$\hat{s} \equiv \hat{s}(s) \tag{3}$$

the average component of $\boldsymbol{F}(s)$ along the migration path with length $l$ reads

$$F = \int_0^l \mathrm{d}s\, \hat{s} \cdot \boldsymbol{F}(s)P(s) \tag{4}$$

with

$$\int_0^l \mathrm{d}s\, P(s) = 1.$$

It is precisely this component of the driving force that will contribute to, for instance, a concentration gradient in an electromigration experiment. This component can be called 'the phenomenological part of the driving force'. For polycrystalline samples the right-hand side of equation (4) should be averaged over all different orientations of the system with respect to the field direction $\hat{E}$. Equivalently the averaging can be performed over all different directions of $\boldsymbol{E}$ with respect to the orientation of the system. In practice this leads to averaging over all forward field directions around $\hat{s}$. After substitution of $\boldsymbol{F}(s) = \underline{Z}^*(s)e\boldsymbol{E}$ into (4) and averaging, the result is

$$F = Z^*eE = \left(\int_0^l \mathrm{d}s\, \hat{s} \cdot \underline{Z}^*(s)\hat{s}P(s)\right)eE. \tag{5}$$

Here $Z^*$ stands for the effective valence as determined from experiment. For the electromigration wind valence it holds that

$$Z_{\mathrm{wind}} = \int_0^l \mathrm{d}s\, \hat{s} \cdot \underline{Z}_{\mathrm{wind}}(s)\hat{s}P(s) \equiv \int_0^l \mathrm{d}s\, Z_{\mathrm{wind}}(s)P(s) \tag{6}$$

given a migration path $s$.

There remains the question of what to take for $P(s)$ along the path. A path-normalized harmonic oscillator ground-state probability density

$$P(s) = (1/N_{\text{path}}) \exp(-M\omega_0 s^2/\hbar) \tag{7}$$

offers a possibility with experimentally determined values for the energy spacing $\hbar\omega_0$, $N_{\text{path}}$ a normalization constant and $M$ the partricle mass. Impurities in their ground state sometimes are approximated as oscillating in a harmonic potential [26]. Values for $\hbar\omega_0$ of typically some 60 to 120 meV correspond to fairly high temperatures (700 K to 1400 K) at which the first excited state becomes populated. It will be seen that the different values of $\hbar\omega_0$ for H and D will result in an isotope effect in the wind valence.

The inclusion of several different migration paths (e.g. the [1 1 0] direction besides the [1 1 1] direction in Pd(H)) also would proceed via (7), but with a different normalization constant. If both paths are walked a weighted average (i.e. 8 times the [1 1 1] contribution and 12 times the [1 1 0] contribution in the case of Pd(H) constitutes the end result.

A physical picture emerges as suggested earlier by Wipf in the context of microscopic diffusion measurements [27]. An interstitial hydrogen atom experiences a driving force of order $F = Z^*eE \approx +1 \cdot e \cdot 10\ \text{V m}^{-1}$. In Pd(H) [28] the harmonic force constant is of order $10\ \text{N m}^{-1}$ and the driving force on the hydrogen atom would be balanced at a displacement of $1.6 \times 10^{-19}$ m from the origin along the field direction, which is negligible. An individual diffusion step will not be influenced at all by the additional force. Note however that a sample length of $5 \times 10^{-2}$ m implies a difference in chemical potential of 0.5 eV (≈5800 K) over the sample. At 900 K a steady state in which the ratio of the hydrogen concentrations in both ends of the sample is of order $e^{5800/900} \simeq 600$ will be reached. Thus the diffusive motion of an ensemble of hydrogen atoms in a metal eventually will be affected when observed over a period of time that is large compared with an attempt frequency of $10^{13}$ Hz. In a sample of macroscopic dimensions transport of hydrogen towards the cathode ($Z^* > 0$) is the tangible result.

### *3.2. Potentials*

The electrons in the host metal are thought to occupy single-particle Bloch states. Application of the KKR formalism, as described in I, yields such Bloch states. To this end the crystal potential is modelled by an array of muffin-tin (MT) potentials. These potentials can be constructed self-consistently [29]. Another approach [30] starts from relativistic, self-consistent atomic charge densities calculated with the aid of a computer program by Desclaux [31]. The Coulomb potential for an electron in an atom is given by

$$V^{\text{c}}_{\text{at}}(r) = -2Z/r + U(r) \tag{8a}$$

where $Z$ denotes the nuclear charge and $U(r)$ is the Hartree potential. The Poisson equation connects $U(r)$ to the atomic electronic charge density $\rho_{\text{at}}(r)$. The exchange interaction is accounted for by adding the atomic Slater exchange potential

$$V^{\text{x}}_{\text{at}}(r) = -6\alpha\{[3/(8\pi)]\rho_{\text{at}}(r)\}^{1/3} \tag{8b}$$

to the Coulomb potential. The exchange parameter $\alpha$ was set equal to 1.

Inside a MT sphere in the crystal the spherically symmetric contributions to the charge density from the first 13 shells of surrounding atoms are added up and used to construct the crystal exchange potential using the crystal analogue of (8*b*). Outside a MT sphere, in the interstitial region, a similar procedure is followed but now the result is a flat

potential, which is approximated by a constant potential called the MT zero. Phase shifts calculated from those MT potentials together with information on the crystal structure serve as input for a KKR program.

The potential for the impurity and its perturbed surroundings is constructed in a similar way, leading to sets of impurity phase shifts. Some of the charge density of the impurity will be accommodated inside the MT spheres of the surrounding atoms, thus admitting charge transfer to neighbouring atoms. In general the radii of the MT spheres should be chosen as large as possible under the restriction that they are not allowed to overlap with other MT spheres. The introduction of an impurity introduces a degree of freedom in choosing its MT radius, which was not present for the perfect lattice. On the one hand, a reduced MT radius for the host atoms in favour of the interstitial should remain large enough to guarantee a realistic description of the electronic structure of the metal. On the other, the radius of the interstitial must lead to electron–impurity scattering in agreement with measured residual resistivities and dHvA quantities. A previous study of the dHvA effect in Pd(H) [32] showed that a MT radius of $0.325a$ for Pd and $0.175a$ for H leads to satisfactory results for Pd host properties as well as for electron–impurity scattering. This choice will be adopted for all FCC metals while for the BCC metals a MT radius of $0.335a$ was chosen. In the absence of an interstitial impurity the maximum allowed MT radii are $0.353a$ and $0.433a$ for FCC and BCC metal atoms respectively. Apparently, for BCC systems the required reduction of the host MT radius is much larger than for BCC systems.

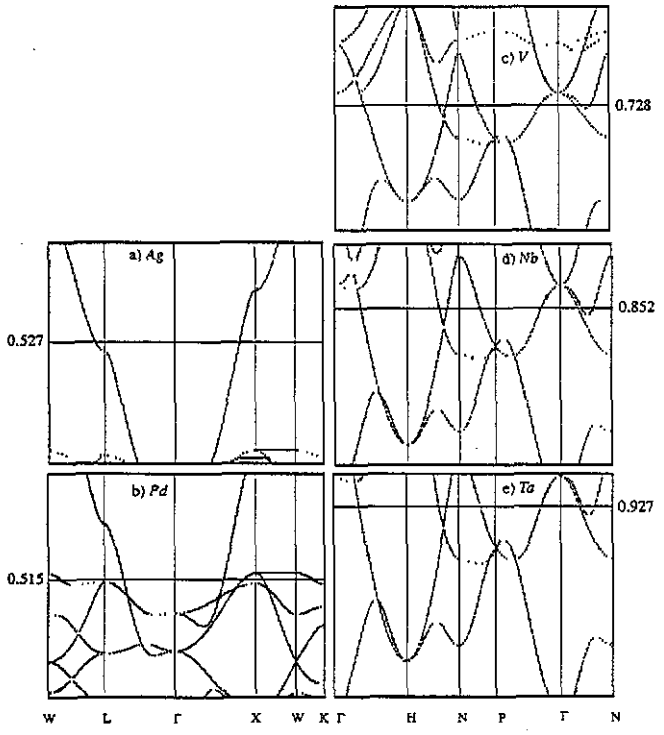


**Figure 2.** Dispersion relations along selected direction in $k$-space for (*a*) Ag, (*b*) Pd, (*c*) V, (*d*) Nb and (*e*) Ta. For Ag and Pd the lowest energy is 0.2 Ryd; for V, Nb and Ta this is 0.5 Ryd. The Fermi level is indicated by the horizontal line.

Figure 2 shows the band structures for Ag, Pd, V, Nb and Ta as obtained from KKR calculations with the host potentials used in the present study of metal/hydrogen systems. The maximum angular momentum was taken at $l = 3$. The band structures in figure 2 compare well with those given by Moruzzi *et al* [29]. In general the agreement for FCC metals is better than for BCC metals, especially when it comes to the density of states (DOS) at the Fermi level, which is too low for the BCC metals. The underlying reason for this can be seen from the way in which the d band crosses the Fermi level along ΓN in $k$-space. The band structure of Moruzzi *et al* indicates smaller velocities and thus a larger DOS at $\varepsilon_F$. Nevertheless, all parts of the Fermi surface are always present and have acceptable shapes and sizes. It is noteworthy that band structures for BCC metals with the larger MT radius are in better agreement with the self-consistent results of Moruzzi *et al*. For the FCC metals the band structures at the maximum MT radius and at the smaller one compare equally well.

Table 2 summarizes some characteristics of the crystal potentials used for the description of the metal/impurity systems considered in this work. A comparison is made with a constructed host potential at the maximum MT radius and with the self-consistent potential of Moruzzi *et al*.

When an interstitial impurity is introduced into a metal it brings along its valence electrons. These extra electrons must be accommodated in scattering states of which the energy is assumed to lie below $\varepsilon_F$. The integrated difference between the DOS before ($N_0(\varepsilon)$) and after ($N(\varepsilon)$) introduction of the impurity, from the bottom of the valence band ($\varepsilon = \varepsilon_0$) up to $\varepsilon = \varepsilon_F$, must equal the total number of newly introduced valence states and equals the number of valence electrons $Z_i$ of the impurity

$$Z_i \equiv \int_{\varepsilon_0}^{\varepsilon_F} d\varepsilon [N(\varepsilon) - N_0(\varepsilon)] \tag{9}$$

This expression can be shown [33] to result in a generalized Friedel sum rule (see I) when elaborated within the framework of the KKR Green function formalism. The impurity potentials used are made to fulfil this sum rule by applying constant energy shifts to them. Such a shift is interpreted as a screening charge smeared out over the surface of a MT sphere [34, 35].

In all cases the impurity itself was left unaltered because it already accommodates some 50% to 80% of the newly introduced charge $-Z_i e$. The rest of the charge was dispersed over the surrounding shell(s) of metal atoms, resulting in shifts varying from $-50$ to $+20$ mRyd. Self-consistent potentials for impurity clusters inherently obey the Friedel sum rule to a larger extent. Unfortunately no such potentials for interstitial impurities are available.

When the impurity traverses a migration path in FCC and BCC metals, thereby leaving its equilibrium position, the MT radius must decrease. An extra amount of charge has to be accommodated on the surrounding metal atoms. This results in a variation of the constant energy shifts along the path but always in such a way that the Friedel sum rule remains constant.

### *3.3. Transport relaxation time*

The $3 \times 3$ wind valence tensor as given by expression (69*a*) in I contains the isotropic transport relaxation time $\tau$ for the conduction electrons. It emerged upon substituting

**Table 2.** Comparison of the DOS per atom $N(\varepsilon_F)$, the average velocity $v_F$, the velocity integral $\frac{1}{4}\int_{FS} dS_k\, v_k$ and the phase shifts $\eta_l$ at the Fermi energy $\varepsilon_F$, for different metals with lattice constant $a$. Except for the phase shifts given in radians, all quantities are in atomic units such that $\hbar = 2m = 1$, $m$ being the electron rest mass. For each metal the first row corresponds to constructed potentials with touching MT spheres (radius $R_{MT}$), the second row to constructed potentials with the smaller MT radius (see text) and the last row to the self-consistent results from [29].

| Metal | $a$ | $R_{MT}$ | $\varepsilon_F$ | $N(\varepsilon_F)$ | $v_F$ | $\frac{1}{4}\int_{FS} dS_k\, v_k$ | $\eta_0$ | $\eta_1$ | $\eta_2$ | $\eta_3$ |
|---|---|---|---|---|---|---|---|---|---|---|
| Cu | 6.831 | 2.415 | 0.584 | 3.55 | 1.16 | 2.45 | −0.044 997 | 0.095 483 | −0.127 750 | 0.001 084 |
| | 6.831 | 2.220 | 0.634 | 3.54 | 1.17 | 2.48 | −0.150 665 | 0.056 347 | −0.149 195 | 0.001 015 |
| | 6.83 | 2.41 | 0.598 | 3.92 | | | −0.059 | 0.096 | −0.145 | 0.001 |
| Ag | 7.722 | 2.730 | 0.471 | 3.39 | 1.44 | 2.41 | −0.098 966 | 0.046 357 | −0.111 678 | 0.001 990 |
| | 7.722 | 2.510 | 0.527 | 3.27 | 1.50 | 2.53 | −0.242 929 | −0.008 866 | −0.138 469 | 0.001 232 |
| | 7.68 | 2.72 | 0.517 | 3.48 | | | −0.189 | 0.025 | −0.149 | 0.003 |
| Ni | 6.694 | 2.367 | 0.594 | 55.2 | 0.259 | 1.07 | −0.197 340 | 0.040 021 | −0.282 086 | 0.001 047 |
| | 6.694 | 2.176 | 0.649 | 49.7 | 0.274 | 1.09 | −0.301 364 | 0.001 685 | −0.324 911 | 0.001 003 |
| | 6.55 | 2.32 | 0.671 | 54.4 | | | −0.280 | 0.020 | −0.324 | 0.001 |
| Pd | 7.351 | 2.599 | 0.448 | 23.4 | 0.543 | 1.43 | −0.318 331 | −0.043 055 | −0.236 897 | 0.001 324 |
| | 7.351 | 2.389 | 0.515 | 22.4 | 0.595 | 1.60 | −0.460 649 | −0.094 864 | −0.298 246 | 0.001 546 |
| | 7.36 | 2.60 | 0.523 | 29.7 | | | −0.393 | −0.064 | −0.311 | 0.002 |
| Al | 7.623 | 2.695 | 0.575 | 3.37 | 2.49 | 7.50 | 0.479 368 | 0.501 103 | 0.058 114 | 0.002 139 |
| | 7.623 | 2.478 | 0.626 | 4.00 | 2.17 | 6.74 | 0.363 039 | 0.422 065 | 0.054 571 | 0.001 866 |
| | 7.60 | 2.69 | 0.618 | 4.78 | | | 0.344 | 0.436 | 0.065 | 0.003 |
| V | 5.713 | 2.474 | 0.612 | 23.4 | 0.467 | 1.87 | −0.623 424 | −0.136 460 | 1.132 046 | 0.001 966 |
| | 5.713 | 1.916 | 0.782 | 18.0 | 0.521 | 1.86 | −0.901 826 | −0.269 198 | 1.052 095 | 0.001 657 |
| | 5.72 | 2.48 | 0.675 | 25.4 | | | −0.691 | −0.173 | 1.030 | 0.003 |
| Nb | 6.238 | 2.701 | 0.656 | 11.8 | 1.01 | 3.51 | −0.894 960 | −0.340 866 | 1.153 463 | 0.006 888 |
| | 6.238 | 2.092 | 0.852 | 6.25 | 2.78 | 8.47 | −1.227 907 | −0.526 527 | 0.897 286 | 0.006 477 |
| | 6.20 | 2.68 | 0.676 | 19.4 | | | −0.932 | −0.363 | 1.142 | 0.007 |
| Ta | 6.238 | 2.701 | 0.720 | 8.24 | 1.50 | 5.24 | −0.985 210 | −0.421 644 | 1.103 099 | 0.008 076 |
| | 6.238 | 2.092 | 0.927 | 4.66 | 3.26 | 9.89 | −1.326 570 | −0.618 080 | 0.822 841 | 0.005 614 |

the widely used approximation

$$\boldsymbol{\lambda}_{nk} = \tau \boldsymbol{v}_{nk} \tag{10}$$

for the vector mean free path $\boldsymbol{\lambda}_{nk}$. Here $\boldsymbol{v}_{nk}$ is the group velocity of an electron in Bloch state $|nk\rangle$. Adopting (10) the bulk conductivity $\sigma$ or inverse bulk resistivity $\rho^{-1}$ for FCC and BCC metals is given by

$$\sigma = \frac{1}{\rho} = \frac{2e^2\tau}{(2\pi)^3\hbar}\frac{1}{3}\int_{\mathrm{FS}} \mathrm{d}S_k \, v_{nk} \tag{11}$$

where the integral is over the Fermi surface. Because $\tau \boldsymbol{v}_{nk}$ is the result of all scattering processes in the metal including the electron–phonon interaction, it accounts for the observed temperature dependence in $\rho$. For a metal with a given electronic structure the only physical, temperature-dependent parameter in the expression for the conductivity is the transport relaxation time $\tau$.

Values for $\tau$ at a given temperature can be deduced from experimental values [36] of $\rho(T)$ and calculated values for the integral in (11). Because the bulk conductivity is a property of the pure metal, the best possible description for the metal is used. In all cases the integral in (11) was evaluated using maximum MT radii. Especially for the BCC metals this leads to markedly different values of the average velocity at the Fermi energy and of the integral in (11) when compared with results pertaining to a smaller host MT radius (see table 2). The electron group velocities have been calculated according to (73*b*) in I from solutions to the KKR equations at energies $\varepsilon_F \pm 10^{-4}$ Ryd.

The values for $\tau$ obtained through (11) incorporate precise information on the shape of the Fermi surface and the electron velocities at the Fermi level. The resulting values can be as much as a factor of 17 larger (Pd) than free-electron relaxation times $\tau_{\mathrm{FE}} = m/(ne^2\rho)$, in which $n$ is the electron density in the metal and $m$ is the electron mass. Although the velocity integral in (11) accounts for the definitely non-spherical shape of the Fermi surfaces of most transition metals, one could question to what extent the isotropic character of $\tau$ can be justified. From expressions (69*c*) and (70) in I one infers that a $\boldsymbol{k}$-dependent relaxation time $\tau_{nk}$ provides an additional weight for the integrand in $\boldsymbol{k}$. Fast decaying fluctuations in the distribution function for the electrons would contribute relatively less to the wind valence (and to the current density). It is known from residual resistivity calculations [37] that upon expressing the vector mean free path as

$$\boldsymbol{\lambda}_{nk} = \tau_{nk}\boldsymbol{v}_{nk} \tag{12}$$

the transport relaxation time for electron–impurity scattering indeed exhibits the aforementioned anisotropy. Unfortunately $\tau_{nk}$ including all scattering processes at a given temperature are not available. One must resort to the cruder approximation of an isotropic $\tau$ and look for comfort in the fact that some anisotropy in the magnitude of $\boldsymbol{\lambda}_{nk}$ is retained through the magnitude of the velocity, varying over the Fermi surface.

The vector mean free path is not affected by inclusion of the electron–phonon interaction via renormalization of the dispersion relation

$$\varepsilon_{nk}^{\mathrm{el\text{-}ph}} - \varepsilon_F = (\varepsilon_{nk} - \varepsilon_F)/(1 + \lambda_{nk})$$

$\lambda_{nk}$ being the electron–phonon enhancement factor [38]. If working with $\boldsymbol{v}_{nk}$ instead of

$$\boldsymbol{v}_{nk}^{\mathrm{el\text{-}ph}} = \boldsymbol{v}_{nk}/(1 + \lambda_{nk})$$

in (11) one ends up with $\tau$ instead of $\tau^{\mathrm{el\text{-}ph}}$ since the Fermi surface itself remains

unchanged. In expression (69*c*) in I the transport relaxation time is then formally recombined with $v_{nk}$ to $\lambda_{nk}$. The fact that the wind force as a whole is not influenced via electron–phonon renormalization is most apparent from the ballistic expression (45*a*) in I, being a limiting case [39] of the more sophisticated expressions for the wind force.

### *3.4. The impurity cluster*

First the moving entity inside the impurity cluster will be defined. The subsections 3.4.2. and 3.4.3. are concerned with the computational details along the migration paths in FCC and BCC metals.

*3.4.1. The migrating entity.* When preparing for actual calculation of the wind valence in electromigration, a confrontation with the difficulty of defining the moving entity along the path seems inevitable. In the KKR MT model this is just the MT sphere containing the impurity nucleus together with a certain amount of negative charge, distributed according to some charge density function. A promising approach towards the problem is to check whether the residual resistivity for the metal/impurity system can be reproduced satisfactorily with the potential chosen for the host and for the impurity cluster. If this indeed is the case, one can infer that an appropriate treatment of the multiple scattering of the electrons at the Fermi energy is guaranteed. The calculation of the residual resistivity [40] involves a detailed knowledge of the alloy wavefunction. It is the local features of this wavefunction, just around the impurity, that enter the calculation of $Z_{\text{wind}}(\boldsymbol{R}_I)$. Therefore in presenting results for the wind valence, residual resistivities corresponding to the same potential will be referred to. The MT radii for the impurity along the migration path are calculated starting from the MT radius at its equilibrium position. The choice of the MT radii for the host and the impurity was discussed in section 3.3, stressing the necessity to retain a reliable description of the host. Now a nice feature of this choice regarding the impurity potential will be brought forward. In both FCC and BCC systems the constructed impurity potential could be used without applying a constant energy shift. Of course a smaller MT radius of the impurity potential might lead to a better description of the host metal while the scattering power of the central impurity strongly decreases. Then a large negative constant energy shift would be required to compensate for this effect but this corresponds to an unphysical amount of screening charge on the central impurity, which should be avoided.

*3.4.2. FCC systems.* In the FCC metals the equilibrium position of the impurity is the octahedral site (see figure 1(*a*)) surrounded by a first shell of six metal atoms and a second shell of eight atoms. As already stated in subsection 3.1 these surrounding atoms are unable to follow the rapidly oscillating impurity (hydrogen) and therefore reside at positions slightly shifted outward in a radial direction. In FCC metals possible directions for migration are the [1 1 0] direction and the [1 1 1] direction. Along the [1 1 0] direction the impurity wavefunction will be strongly localized at the octahedral site and it is only for positive muons that sometimes the [1 1 0] path is adopted [41]. In general interstitial impurities in FCC metals at elevated temperatures are assumed to migrate by an over-barrier jump via the tetrahedral position to a neighbouring octahedral site (see figure 1(*a*)). This is confirmed by microscopic studies based on nuclear magnetic resonance (NMR) [42] and quasielastic neutron scattering (QNS) [43] techniques. In the present work the migration path will be taken in the [1 1 1] direction. In an earlier publication [44] the [1 1 0] path was always included, weighted by the proton probability in this direction.

Because of the low probability of finding the proton in the region where the differences in wind valence along the [1 1 1] and [1 1 0] directions become significant, the end result was only affected slightly by including the [1 1 0] path.

Along the [1 1 1] path the wind valence tensor was calculated at seven points. Point number 0 is the octahedral site while point number 4 corresponds to the smallest interstitial MT radius. In the calculations for the first four points the same (if available, experimental) lattice distortion for the first shell was assumed. The last two points (5 and 6) are located inside a tetrahedron of four surrounding atoms with an estimated or calculated [23] lattice distortion. At the narrow point (number 4) several possibilities for lattice distortion are available but the influence on the already small matrix elements of $\underline{Z}_{\text{wind}}(\boldsymbol{R}_l)$ is not very large. It should always be borne in mind that the influence on the final scalar wind valence (see equation (6)) of such points, where the proton probability density is small, is marginal. It is therefore gratifying that the more remote points, where the environmental details are not known, are those that contribute least. This includes the tetrahedral site for which no bound proton or deuteron state has ever been reported.

Things really matter in the vicinity of the octahedral site. When the impurity moves towards the tetrahedral site the six first-shell atoms are split up into two classes of inequivalent atoms. Accordingly combinations of two different constant energy shifts might apply in order to fulfil the Friedel sum rule, introducing an extra degree of freedom. This feature was tackled in the following way. A calculation at point 0, at a given lattice distortion, yields a constant energy shift $\delta\varepsilon_0$ for all six equivalent surrounding atoms. At points 1 to 3 the wind valence was calculated using either (i) $\delta\varepsilon_0$ for the three atoms in the [$\bar{1}\bar{1}\bar{1}$] direction and searching for fulfilment of the Friedel sum rule through adjustment of the potential for the three atoms in the [1 1 1] direction, or (ii) an equal energy shift for all six atoms as if they were equivalent. The largest differences between (i) and (ii) were 1%, 4% and 20% with respect to (i) for positions 1, 2 and 3 respectively in Cu(H). In all other FCC metals the differences are an order of magnitude smaller, probably because of their larger lattice constant. The values obtained according to method (i) are used to calculate the scalar wind valence because they incorporate some features of a cloud of screening electrons following the impurity adiabatically.

*3.4.3. BCC systems.* For BCC metal/hydrogen systems the tetrahedral position (point group $D_{2d}$) is generally accepted as the equilibrium position of the proton although some doubt exists concerning the V(H) system at higher hydrogen concentrations [45, 46]. Figure 1(*b*) shows two tetrahedral sites on one of the faces of a BCC unit cell. Additionally there are octahedral sites (point group $D_{4h}$) which are believed to be the equilibrium positions for impurities like C, N and O. A tetrahedral site has a first and second shell both of four surrounding atoms, while an octahedral site has a first shell of two and a second shell of four atoms.

In BCC metals the distance between two tetrahedral sites is, roughly speaking, a factor of 2 smaller than the distance between two octahedral sites in an FCC metal. Reported activation energies for hydrogen diffusion in BCC metals at elevated temperatures are a factor of 2 to 5 lower when compared to FCC data. As a consequence the jump rates for hydrogen are relatively high. Mössbauer spectroscopy studies on the Ta(H) system [47] revealed jump rates of $1.04 \times 10^{11}$ Hz at room temperature whereas the ground-state oscillator frequency for the hydrogen atom is approximately $3 \times 10^{13}$ Hz. QNS experiments ($T > 550$ K) on the hydrides of V, Nb and Ta showed systematic deviations from predictions based on a simple nearest-neighbour jump model [25]. Agreement between

theory and experiment has been obtained in a model that assumes correlated jumps in the [1 1 0] direction. At room temperature the experimental data could be explained by a simple nearest-neighbour jump model in which the hydrogen atom jumps between two tetrahedral sites along the [1 1 0] direction. Such experiments on a microscopic scale further showed that the proton can still be considered as localized at an interstitial site [25]. Speculations on extended proton states (four tetrahedral sites: 4T states) in the context of superdiffusion [48] of H in V could be falsified [49].

From the foregoing discussion it can be concluded that hydrogen diffusion at normal temperatures in BCC metals certainly is less well understood than for FCC metals. For the purpose of the wind valence calculations the picture of a hydrogen atom oscillating in a bound state located at the tetrahedral site and migrating towards a neighbouring site will be adopted. As will be seen in the following section the assumption of a straight migration path leads to the *wrong sign* for the electromigration wind valence of hydrogen in Nb and Ta. For a curved path (see figure 1(*c*)), along which the proton probability density takes an extreme value [23], the calculated results are in agreement with experiment. The shape of the proton probability density is a reflection of the potential in which the proton moves. When this potential is taken to be the sum of four metal–hydrogen pair potentials it is immediately clear that the [1 1 0] path is not a classical minimum energy path.

Because points along such a curved path have a very low symmetry (point group $C_s$), the path in the [1 0 0] direction (point group $C_{2v}$) is taken as an approximation. Migration then takes place via the octahedral position. This should simulate the actual path closely because the tetrahedral position and points not too far from this position are approximated quite well by the [1 0 0] path. These points will be weighted most heavily by the proton probability density in the final scalar wind valence.

Wind valence calculations are performed at five equidistant points along the [1 0 0] direction, point 0 being the tetrahedral site. The lattice distortion around the equilibrium position is known experimentally [50] and is in reasonable agreement with theoretical investigations [23]. The points 0, 1 and 2 are treated as surrounded in this way. Lattice distortion around the octahedral site was taken from the work of Puska and Nieminen [23] and applied to the points 3 and 4 as well as to point 2. The difference in the wind valence between the tetrahedral and octahedral approach of point 2 was always less than 5%. In order to fulfil the Friedel sum rule the same strategy was used as described for the FCC systems. It turned out that, owing to the smaller impurity–metal atom distance, there was no need to differentiate between inequivalent atoms in the surrounding shells.

## 4. Results

The results of actual wind valence calculations in FCC and BCC metals are discussed in subsections 4.1 and 4.2 respectively. All calculations include the effect of a first shell of perturbed host atoms around the equilibrium position of the interstitial. Table 3 displays the lattice distortion of the first shell as well as the interstitial MT radius. The phase shifts as given for each system satisfy the generalized Friedel sum rule. Results on the wind valence in various systems are summarized in table 4. An impression of the influence of lattice distortion of the first shell on the wind valence at the equilibrium position is given in table 5.

The influence of a second shell of perturbed host atoms turned out to be negligible for the case of interstitial hydrogen. This feature was noticed before in a study of dHvA

**Table 3.** Column two shows the interstitial MT radius, column three shows the radial outward displacement of the first-shell atoms as a percentage of the lattice constant. The phase shifts $\eta_l$ are those used for the interstitial at its equilibrium position (first row) and for the first shell of surrounding atoms (second row). The Friedel sum rule is fulfilled for these impurity cluster data.

| System | $R^I_{MT}$ | $100\delta r/a$ | $\eta_0$ | $\eta_1$ | $\eta_2$ | $\eta_3$ |
|---|---|---|---|---|---|---|
| Cu(H) | 1.195 | 2.0 | 1.230 710 | 0.028 273 | 0.000 550 | 0.000 007 |
| | | | −0.119 113 | 0.070 678 | −0.139 695 | 0.001 104 |
| Ag(H) | 1.351 | 1.0 | 1.359 492 | 0.031 699 | 0.000 639 | 0.000 009 |
| | | | −0.206 046 | 0.006 548 | −0.132 598 | 0.002 286 |
| Ni(H) | 1.171 | 1.0 | 1.184 282 | 0.026 574 | 0.000 511 | 0.000 006 |
| | | | −0.280 858 | 0.010 368 | −0.302 328 | 0.001 067 |
| Pd(H) | 1.286 | 1.0 | 1.259 393 | 0.024 300 | 0.000 440 | 0.000 005 |
| | | | −0.449 454 | −0.091 029 | −0.291 267 | 0.001 591 |
| Pd(B) | 1.286 | 2.5 | 0.704 972 | 0.425 585 | 0.002 187 | 0.000 023 |
| | | | −0.378 271 | −0.066 882 | −0.241 985 | 0.001 854 |
| Pd(C) | 1.286 | 2.0 | 1.501 023 | 1.240 049 | 0.002 452 | 0.000 025 |
| | | | −0.402 249 | −0.074 825 | −0.262 249 | 0.001 774 |
| Al(H) | 1.334 | 1.0 | 1.260 470 | 0.036 453 | 0.000 854 | 0.000 014 |
| | | | 0.404 316 | 0.469 235 | 0.059 931 | 0.002 093 |
| V(H) | 1.278 | 4.0 | 1.157 341 | 0.043 176 | 0.001 188 | 0.000 022 |
| | | | −0.896 909 | −0.267 355 | 1.163 995 | 0.001 698 |
| Nb(H) | 1.395 | 3.0 | 1.164 623 | 0.060 603 | 0.002 139 | 0.000 051 |
| | | | −1.220 613 | −0.522 695 | 0.998 140 | 0.006 706 |
| Nb(C) | 1.027 | 5.0 | 0.772 647 | 0.707 782 | 0.002 775 | 0.000 031 |
| | | | −1.209 075 | −0.519 634 | 1.150 912 | 0.007 203 |
| Nb(O) | 1.027 | 5.0 | −1.391 999 | −0.789 074 | 0.003 048 | 0.000 032 |
| | | | −1.210 152 | −0.519 683 | 1.127 329 | 0.007 133 |
| Ta(H) | 1.395 | 2.5 | 1.109 885 | 0.064 301 | 0.002 489 | 0.000 065 |
| | | | −1.317 238 | −0.612 652 | 0.926 601 | 0.005 978 |

quantities in Pd(H) by Oppeneer *et al* [32] as well as in the calculation of residual resistivities [40].

Subsection 4.3 is an attempt to reveal the actual nature of the wind force by taking a closer look at the field-induced charge density just outside the MT sphere of the interstitial. The H/D isotope effect in $Z_{wind}$ and $Z^*$ are discussed in subsection 4.4. Temperature effects due to the broadening of the energy derivative of the Fermi–Dirac distribution function are estimated in subsection 4.5.

### *4.1. FCC systems*

*4.1.1. Cu(H) and Ag(H).* As expected the shapes of the $Z_{wind}(s)$ versus $s$ curves (see equation (6)) for Cu(H) and Ag(H) are much alike. Figure 3(*a*) shows this relation for Ag(H). Inclusion of lattice distortion and charge transfer (full-curve) results in a slight lowering of the wind valence along the path when compared to just a hydrogen atom in the perfect lattice (dotted curve). It is clear that in the latter case the Friedel sum criterion

**Table 4.** Results of the wind valence calculations for various systems. Columns 2 and 3 display the wind valence at the equilibrium position with and without surrounding atoms. Columns 4 and 5 give the wind valences for hydrogen and deuterium as obtained from averaging over the probability density for a harmonic potential at energies (in meV) shown in column 7 ($\hbar\omega_0^D = \hbar\omega_0^H/\sqrt{2}$). The transport relaxation time (in atomic units: 1 au = $4.8378 \times 10^{-17}$ s) is given in column 6. The last two columns are wind valences obtained from the ballistic formula with calculated residual resistivities including or excluding environmental effects.

| | $Z_{wind}(0)$ | | | | | | $Z_{wind}^{ballistic}$ | |
|---|---|---|---|---|---|---|---|---|
| System | First shell | Imp. only | $Z_{wind}^H$ | $Z_{wind}^D$ | $\tau$ | $\hbar\omega_0^H$ | First shell | Imp. only |
| Cu(H) | −29.3 | −25.6 | −23.5 | −24.8 | 163 | 120 | −28.8 | −24.9 |
| Ag(H) | −36.5 | −34.6 | −31.9 | −32.9 | 211 | 106 | −41.2 | −39.7 |
| Ni(H) | −0.07 | −0.15 | −0.07 | −0.07 | 74 | 115 | −22.1 | −0.03 |
| Pd(H) | −0.75 | −0.68 | −0.43 | −0.49 | 61 | 60 | −16.6 | −0.03 |
| Pd(B) | −0.36 | −0.06 | | | 61 | | −75.5 | −0.96 |
| Pd(C) | −0.76 | −0.16 | | | 61 | | −82.7 | −2.24 |
| Al(H) | −1.1 | −1.3 | −1.15 | −1.13 | 36 | 51 | −2.4 | −1.5 |
| V(H) | 0.22 | 0.21 | 0.17 | 0.19 | 53 | 120 | −28.7 | −4.8 |
| Nb(H) | 1.68 | 2.44 | 1.78 | 1.75 | 42 | 110 | −29.4 | −6.0 |
| Nb(C) | 0.27 | −0.56 | | | 10 | | | |
| Nb(O) | −1.6 | −0.68 | | | 10 | | | |
| Ta(H) | −0.66 | −0.36 | −0.56 | −0.59 | 28 | 120 | −20.4 | −3.6 |

**Table 5.** Influence of lattice distortion of the first shell on the wind valence of a hydrogen atom at its equilibrium position. The second column displays the wind valence in the absence of environmental effects. The lattice distortion as a percentage of $a$ is given in the headings to columns 3 to 8.

| | $Z_{wind}(0)$ | | | | | | |
|---|---|---|---|---|---|---|---|
| System | Imp. only | 0% | 1% | 2% | 3% | 4% | 5% |
| Ag(H) | −34.6 | −34.7 | −36.5 | −38.6 | −40.9 | | |
| Pd(H) | −0.68 | −0.67 | −0.75 | −0.83 | −0.93 | | |
| Nb(H) | 2.44 | 2.11 | 2.00 | 1.82 | 1.68 | 1.52 | 1.34 |
| Ta(H) | −0.36 | −0.36 | −0.52 | −0.63 | −0.69 | −0.73 | −0.75 |

cannot be satisfied. For Cu(H) this lowering is larger than it is for Ag(H), which can be understood from the difference in lattice constants of Cu and Ag. The more remote first-shell atoms in Ag are less influenced by the hydrogen atom than those in Cu and will therefore have smaller influence on the wind valence upon inclusion. The maximum in the curves in figure 3($a$) corresponds to the 'narrow point' along the [1 1 1] direction, where most of the hydrogen-induced charge density is located on the three immobile metal atoms closest to the impurity. Owing to the reduced scattering power of the moving entity itself (but not necessarily of the cluster as a whole) the magnitude of the wind

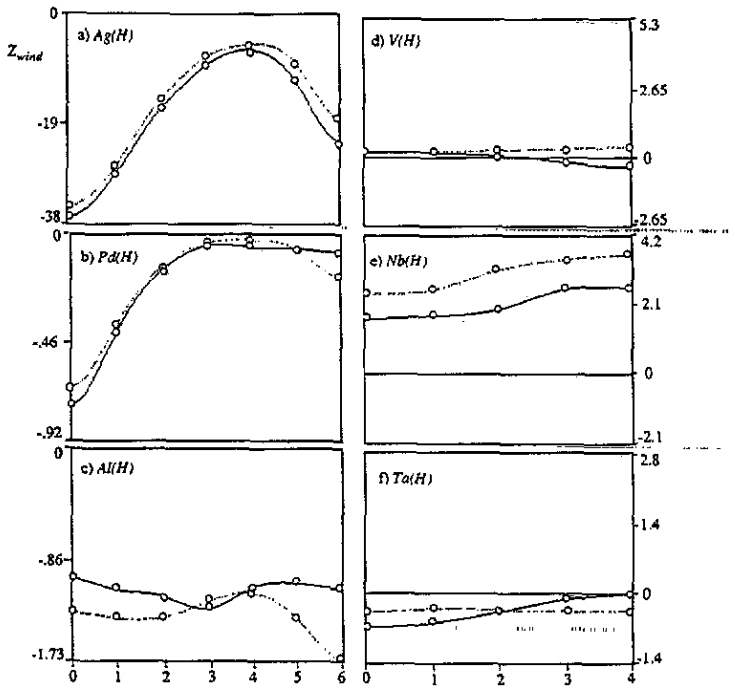


**Figure 3.** Calculated wind valence $Z_{wind}(s_i) \equiv \hat{s}_i \cdot \underline{Z}_{wind}(s_i)\hat{s}_i$ at equidistant points $i$ along the path for the FCC metal/hydrogen systems (*a*) Ag(H), (*b*) Pd(H) and (*c*) Al(H), and the BCC systems (*d*) V(H), (*e*) Nb(H) and (*f*) Ta(H). The spline interpolation (full curve) is through points including environmental effects while the dotted curve results from just the H atom in a perfect lattice.

valence is a minimum. Upon entering the tetrahedral site the absolute value of the wind valence increases again. The wind valence of hydrogen in Cu and Ag could be seen as being directly proportional to the MT radius of the hydrogen atom along the path. However, as will be seen from the cases of Pd(H) and especially Al(H), this is not true in general.

Comparison with experimental data shows that indeed the large negative wind valences are reproduced for Ag(H) (as well as for Cu(H)) [51]. Concentrating on Ag(H) it can be judged from tables 1 and 4 that the calculated values are a factor of 2 to 4 larger than the effective valences reported by Einziger and Huntington [8]. It has been brought forward [9] that their results might be a factor of 2 too low due to a systematic error in the experimental set-up. This would be in favour of the theoretical result presented here. As far as the huge isotope effect is concerned (see table 1) it is clear from table 4 that a simple zero-point motion model cannot explain the observed ratio $Z^*_H/Z^*_D = 0.38$. In such a model the slightly more localized probability density function (see equation (7)) for the deuteron at the octahedral position provides a heavier weight for the largely negative wind valences around this point than for the proton. This leads to a small H/D isotope effect in the wind valence (see table 4). Oscillator frequencies used here are those estimated by Teichler [52] for Cu(H), which have been scaled by the ratio of lattice constants $a_{Cu}/a_{Ag}$ for use in Ag(H). Even the improbable assumption that the proton, contrary to the deuteron, would reside at the tetrahedral site gives only a ratio of about 0.6.

Table 4 further shows values for the wind valence

$$Z_{\text{wind}} = -100 Z_{\text{host}} \rho_0 / \rho \tag{13}$$

according to the ballistic model of Fiks [53] and Huntington and Grone [54] in which $Z_{\text{host}}$ is the host valence (i.e. 1 for Cu and Ag), $\rho_0$ is the residual resistivity in $\mu\Omega$ cm/at.% and $\rho$ is the bulk resisitivity in $\mu\Omega$ cm. For Cu(H) and Ag(H) these values compare well to the results from the sophisticated calculation. This reflects the free-electron-like shape of the Fermi surfaces of these transition metals.

*4.1.2. Pd(H), Pd(B) and Pd(C).* Inclusion of environmental effects in Pd(H) brings about a marked change in the shape of the curve around the tetrahedral site (see figure 3(*b*)). At the octahedral site the wind valence is lowered by some 10% at the experimental lattice distortion. From table 5 it can be seen that for hydrogen in Pd (as well as in Ag, Nb and Ta) the mere inclusion of the first shell, i.e. without lattice distortion, does not alter the wind valence too much. It is the outward displacement of the surrounding atoms that leads to a lowering of the wind valence, which means a decrease in magnitude for the Nb(H) system. The effect of inclusion of the first shell on $Z_{\text{wind}}$ is limited in Pd(H) in sharp contrast with the effect on $\rho_0$. The residual resistivity due to hydrogen is enlarged by a factor of 400 when the first shell is accounted for [40]. This means that in the real Pd metal the local situation at the interstitial site, being probed by $Z_{\text{wind}}$, is not altered to a large extent while the charge accommodated on the first shell and its lattice distortion cause the main part of $\rho_0$. In a jellium description this would turn out differently. In a jellium the hydrogen charge density located at a distance of approximately $a/2$ might contribute to the scattering cross section of the proton and hence to the wind valence because the proton, including its screening charge, is mobile in all directions. In a real metal part of the screening charge, contributing to the scattering power of the hydrogen, is lost to the immobile surrounding atoms. This immediately explains why the wind valence calculated with the ballistic formula (13) gives results for impurities in Pd that are far too large. In fact one should use something like the part of $\rho_0$ due to the interstitial itself. Although this is an unphysical quantity it can be obtained from a calculation. Such ballistic wind valences based on calculated $\rho_0$ are given in table 4. The last column uses $\rho_0$ from a calculation where just the interstitial is embedded in the perfect Pd crystal while the last but one column uses $\rho_0$ from a complete calculation [6]. It is clear that the huge negative ballistic wind valences are avoided when the $\rho_0$ for the bare interstitial are used.

A small H/D isotope effect is found after application of the zero-point motion model to the Pd(H) curve in figure 3(*b*). The oscillator energies are based on the harmonic approximation for the potential in which the proton moves [28]. It is interesting to comment on the effect of using a weighted average over the migration path with a view to resulting values of $Z_{\text{direct}}$ starting from measured $Z^*$ values. Compared to $Z_{\text{wind}}(0)$, i.e. the value at the octahedral site, $Z_{\text{wind}}$ has a somewhat smaller magnitude and leads to a value of 0.87 for the direct valence of a hydrogen atom in Pd, while $Z_{\text{wind}}(0)$ alone would give $Z_{\text{direct}} = 1.19$. The latter would be a curious result for a proton with nuclear charge +1. Assuming that there is no isotope effect in $Z_{\text{direct}}$ the wind valences

$$Z^{\text{H}}_{\text{wind}} = -0.43 \qquad Z^{\text{D}}_{\text{wind}} = -0.49$$

lead to a larger effective valence for hydrogen than for deuterium in Pd, in agreement

with experiment. From the measured effective valences and the calculated wind valences one finds for the direct valences

$$Z^{H}_{direct} = +0.87 \qquad Z^{D}_{direct} = +0.84$$

in agreement with the conclusion of Verbruggen and Griessen from experiments based on the so-called proton Hall effect [55] that the direct valence of hydrogen in palladium must be close to unity.

Because B and C are heavier than H no zero-point motion averaging needs to be performed. The wind valence at the equilibrium position dominates the average strongly. Wind valences for these atoms in Pd are of the same order of magnitude as for hydrogen (see table 4). According to a recent idea of Lodder [56] the direct valence might be resistivity-dependent and approach the valence $Z_i$ of the interstitial in the high-temperature regime. From this and the valences +3 and +4 for B and C respectively, effective valences of about +3 at 1000 K are predicted.

*4.1.3. Ni(H).* Below the Curie temperature ($T_C$ = 627 K) Ni exhibits ferromagnetism. The electromigration experiments were carried out at temperatures $T > T_C$ allowing for a paramagnetic treatment of the nickel host. The residual resistivity of Ni(H) has been accurately determined but, of course, in ferromagnetic Ni. The theoretical value for $\rho_0$ at 1% lattice distortion [40], however, was found to be close to the experimental value, perhaps indicating the relative unimportance of magnetism in Ni when describing electron–impurity scattering.

As in the case of Pd(H) a huge increment of $\rho_0$ upon adding the first shell was found while the wind valence at the octahedral site changed from −0.15 to −0.07 (table 4). After averaging with $\hbar\omega_0^H = 115$ meV [23] and $\hbar\omega_0^D = 115/\sqrt{2}$, for both H and D a small wind valence of −0.07 was found.

Although the experiments on Ni(H) were also criticized by Wipf and Erckmann [9] in that the effective valences obtained for H and D at 750 K are too low, values for the direct valence comparable to those in Pd(H) are found

$$Z^{H}_{direct} = +0.67 \qquad Z^{D}_{direct} = +0.83.$$

The maximum correction factor of 2 as proposed by Wipf and Erckmann would lead to $Z^*$ values larger than unity, incompatible with negative wind valences predicted by the theory in view of a physically expected maximum of +1 for $Z_{direct}$. Further it is interesting to note that upon going from Ni to Pd the wind valence increases as is found for the Cu/Ag combination. This is probably related to the increase in lattice parameter allowing for a larger interstitial MT sphere. Less of the hydrogen charge density (i.e. scattering power) will be lost to the first shell upon an increase of the lattice parameter.

*4.1.4. Al(H).* The solubility of hydrogen in Al is extremely low [20], which is a complicating factor when designing an experimental set-up. Until now no experimental data on the effective valence nor on the residual resistivity of hydrogen in Al are available. It is a straightforward exercise to determine the wind valence of an interstitial in Al being a trivalent simple metal. Information on lattice distortion and $\hbar\omega_0$ values were taken from the effective-medium calculations on Al(H) by Puska and Nieminen [23].

The wind valence curve for Al(H) along the [1 1 1] path exhibits an encouraging feature, namely an increasing magnitude of the wind valence with a decreasing interstitial MT radius. This is reassuring for, from the results presented so far, one might assert that any variation of the wind valence along the path is simply induced by the MT radius of

the interstitial in a sense that a smaller scatterer automatically will lead to a lessening of the magnitude of the wind valence. The example of Al(H) clearly demonstrates that this need not be the case.

At 900 K wind valences of $-1.15$ and $-1.13$ were found for the proton and the deuteron respectively. The virtual absence of an isotope effect is a consequence of the modest variation of $Z_{\text{wind}}(s)$ along the path. It is expected that the effective valence for a hydrogen atom in aluminium will be close to zero, thereby assuming a direct valence of about unity.

### 4.2. BCC systems

The BCC metal/hydrogen systems are well investigated and show some intriguing features in electromigration. From the temperature dependence of $Z^*$ it must be concluded that the hydrogen wind valence in V(H) and Nb(H) has a positive sign, opposite to what is found for Ta(H) [2, 12]. Positive wind valences are sometimes interpreted as being connected to so-called hole conduction, which is reflected in the sign of the Hall coefficient (see table 1). Ta having the largest positive Hall coefficient, however, has a negative wind valence. In addition the most important part of the Fermi surface in V, Nb and Ta is the so-called jungle gym around a band minimum (see figure 2) where the current carriers behave like electrons. Obviously the picture that invokes the scattering of positive and negative charge carriers in a metal is not useful.

*4.2.1. V(H).* For the description of the vanadium host metal atomic charge densities were used from a self-consistent field (SCF) calculation with the experimental $[Ar]3d^34s^2$ ground-state configuration. Regarding this choice Moruzzi *et al* [29] are referred to, for they report a difference between the local density ground state ($[Ar]3d^44s^1$) and the experimental ground state which was not observed for Nb atomns. The alternative $[Ar]3d^44s^1$ configuration resulted in the wrong sign of the wind valence although reasonable values for the residual resistivity in V(H) were found. At the experimental lattice distortion around the hydrogen atom at the tetrahedral site, the $[Ar]3d^34s^2$ host resulted in residual resistivities that are a factor of 2 larger. This dependence of the electronic structure of vanadium on the atomic configuration used to construct the crystal potential was already noted by Matheiss [30].

Figure 3(*d*) show the wind valence along the [1 0 0] path. averaging with the harmonic probability density along the path at energies $\hbar\omega_0^{\text{H}} = 120$ meV and $\hbar\omega_0^{\text{D}} = 85$ meV, wind valences

$$Z^{\text{H}}_{\text{wind}} = +0.17 \qquad Z^{\text{D}}_{\text{wind}} = +0.19$$

are obtained. Obviously these values are too small for they would lead to direct valences of about $+1.5$, which is an unphysical result. Clearly the MT description of an interstitial in vanadium suffers from shortcomings. Although there is some uncertainty about the best choice for the host potential, the DOS at $\varepsilon_{\text{F}}$ compares well with self-consistent KKR results (see table 2). Probably the rearrangement of the charge density around the proton in the vanadium lattice, having a relatively small lattice constant, was not accounted for properly in the construction method described in section 3.5.

*4.2.2. Nb(H).* Averaging of the $Z_{wind}(s)$ curve (figure 3(*e*)) at energies of 110 meV and $110/\sqrt{2}$ meV leads to wind valences

$$Z^{H}_{wind} = +1.78 \qquad Z^{D}_{wind} = +1.75.$$

The [Kr]$4d^4 5s^1$ experimental ground-state configuration used for the Nb atom leads to a crystal potential that gives $\rho_0$ values which compare nicely with experimental resistivity changes [40].

It is extremely interesting to see how these positive values for $Z_{wind}(s)$ come about. The wind valence tensor at the tetrahedral site has the shape

$$\underline{Z}_{wind}(0) = \begin{pmatrix} 1.68 & 0 & 0 \\ 0 & -5.03 & 0 \\ 0 & 0 & -5.03 \end{pmatrix}.$$

When this tensor is sandwiched between unit vectors in the [1 1 0] direction (see equation (6)) the result is $Z_{wind} = -1.68$. A positive wind valence is obtained only when leaving the tetrahedral site along directions close to the [1 0 0] direction. This can be seen as an independent proof of the fact that a diffusion step takes place via a curved path and not along a straight line in the [1 1 0] direction.

The wind valences quoted above strongly suggest a direct valence close to unity for hydrogen in Nb. This is in agreement with the experimental observation of Erckmann and Wipf [12] that the effective valence tends towards unity from above as a function of increasing temperature. For deuterium one finds $Z_{direct} = 0.65$, which would imply a considerable isotope effect in the direct valence. Verbruggen *et al* [2] found $Z_{direct} = 0.4 \pm 0.1$ from an extrapolation to infinitely large resistivity (i.e. $\tau \to 0$) in Nb samples containing approximately 1 at.% hydrogen. It is worth mentioning that the measured $Z^*$ increases with decreasing H concentration [12]. Together with the calculated wind valences this would lead to larger $Z_{direct}$ values.

The equilibrium position of interstitial oxygen in Nb is assumed to be the octahedral site [21]. With a radial outward displacement of $0.05a$ and $0.01a$ of the first and second shells respectively, one finds a wind valence $Z_{wind} = -1.6$ for $\tau = 10$ au at 2400 K (see table 4). At the tetrahedral site with 3.5% lattice deformation $Z_{wind} = -5.1$. For an octahedral oxygen atom with a direct valence between 0 and +1.6 this indeed would result in migration towards the anode (i.e. $Z^* < 0$). The temperature dependence of $Z^*$ however suggests a positive wind valence.

Carbon in Nb at the octahedral or tetrahedral site, with the same lattice distortion as assumed for oxygen, resulted in wind valence values of +0.27 and −6.3 respectively. The octahedral result is compatible with $Z^* \simeq 2.6$ at 2400 K when taking $2 \leqslant Z_{direct} \leqslant 4$ according to the number of valence electrons in the carbon atom. The tetrahedral wind valence certainly would result in migration towards the anode, in clear contradiction with experiment.

*4.2.3. Ta(H).* As for vanadium the experimental $d^3s^2$ atomic ground state was used to construct the crystal potential. The residual resistivity of interstitial hydrogen in Ta, using the [Xe]$4f^{14}5d^36s^2$ configuration, is in good agreement with experiment [40]. The band structures of Nb and Ta are much alike (figure 2), reflecting that a common crystal structure leads to a similar $\varepsilon_{nk}$ versus $k$ relation. From this alone such a striking difference in the wind valence as depicted in figures 4(*e*) and (*f*) for Nb(H) and Ta(H), respectively, is certainly not comprehensible. The similarity of the dispersion relation in Nb and Ta

has always formed the basis of the assertion that the electronic structures of both metals must be much alike.

Averaging over the proton and deuteron probability density yields

$$Z^{H}_{wind} = -0.56 \qquad Z^{D}_{wind} = -0.59$$

again strongly suggesting a direct valence of +1 for hydrogen in Ta. Verbruggen *et al* [2] found $Z_{direct} = 1.2 \pm 0.1$ at $c_H \simeq 0.01$. The negative wind valence in Ta comes about in the same way as the positive wind valence for Nb(H) but now via a negative $xx$ component of the wind valence tensor, at $s = 0$ reading as

$$\underline{Z}_{wind}(0) = \begin{pmatrix} -0.66 & 0 & 0 \\ 0 & 0.81 & 0 \\ 0 & 0 & 0.81 \end{pmatrix}.$$

For a more detailed study of the remarkable difference in the wind valence of H in Nb or Ta the contributions of the different sheets of the Fermi surface at the tetrahedral position are given below:

Nb $\qquad Z^{central}_{wind}(0) = -0.19 \qquad Z^{j.gym}_{wind}(0) = +1.87$

Ta $\qquad Z^{central}_{wind}(0) = -0.04 \qquad Z^{j.gym}_{wind}(0) = -0.63.$

Important observations can be made. First, the contribution due to the second-zone central sheet enclosing holes at $\Gamma$ is relatively small and negative in both systems. The main effect in both cases is due to the much larger third-zone jungle gym sheet of the Fermi surface. Secondly, the difference in the sign of $Z_{wind}$ is due to the jungle gym sheet giving a large positive contribution for Nb(H) but a negative contribution for Ta(H). In both cases the electrons at this sheet have a d-like character. The fact that the $5d^36s^2$ configuration was used for Ta and the $4d^45s^1$ configuration for Nb is not essential, for the Ta $5d^46s^1$ results give qualitatively the same picture. The magnitude of the wind valence turned out to be approximately a factor of 2 larger.

Two possible causes for the difference between Nb and Ta remain, namely (i) Nb has a Kr noble-gas configuration below its valence shell whereas Ta has a $[Xe]4f^{14}$ core, and (ii) the relativistic treatment of atomic Ta ($Z = 73$) will certainly be of more importance than for Nb ($Z = 41$). In the following section it will be investigated whether these two points can be connected with calculated differences in the charge density (at $\varepsilon_F$) around the impurity. Of course, in reciprocal space where Nb and Ta indeed are much alike, such local information is not available.

### *4.3. Charge density at $R_{MT}$*

Now that hydrogen wind valences have been obtained that suit experimental data in a consistent way it is instructive to investigate the basic nature of the wind force. Of course the wind force emerges from $\delta\rho(x)$, the alteration of the charge density around the impurity at $x = 0$ induced by the electric field $E$,

$$\delta\rho(x) = -e \sum_{nk} [f(\varepsilon_{nk}) - f_0(\varepsilon_{nk})] |\bar{\Psi}_{nk}(x)|^2 \tag{14}$$

with $f(\varepsilon_{nk}) - f_0(\varepsilon_{nk})$ the non-equilibrium part of the distribution function $f(\varepsilon_{nk})$. The square of the alloy wavefunction $\bar{\Psi}_{nk}(x)$ can be elaborated within the KKR Green function

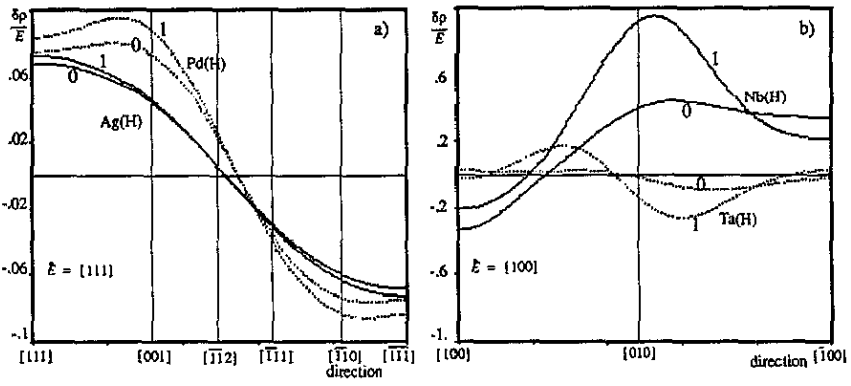


**Figure 4.** Field-induced charge densities on the MT sphere in varying directions. In (*a*) the full curves are for the Ag(H) system and should be multiplied by a factor of 50. The numbers 0 and 1 indicate calculations without and with environmental effects respectively. The dotted curves correspond to the Pd(H) system. In (*b*) the full and dotted curves correspond to Nb(H) and Ta(H) respectively.

approach (see I). After conversion of the summation over Bloch states in (14) to an integral over the Fermi surface the result is

$$\delta\rho(x) = -e^2 \sum_{L,L'} R^*_{lL}(x)(W_{LL'} \cdot E)R_{lL'}(x). \tag{15}$$

The regular solutions $R_{lL}(x)$ pertaining to the impurity potential and the vectorial matrix $W_{LL'}$ are discussed extensively in I. The angular momentum summation ($L \equiv (l, m)$) will have converged to a large extent with $l_{max} = 3$ because at the small interstitial MT radius, where $\delta\rho(x)$ will be evaluated, the spherical Bessel function $j_4(\varepsilon_F^{1/2} R_{MT})$ in $R_{lL}$ ($l = 4$) is already small. Sorbello previously evaluated this quantity within the frame of a pseudopotential treatment of the wind force [57]. From his work it is seen that $\delta\rho(x)$ slowly oscillates as a function of $x$. The charge density variation $\delta\rho(x)$ will be evaluated at $x = R_{MT}$ and it is assumed that this provides a picture of the net behaviour of $\delta\rho(x)$ from $x = 0$ to $x = R_{MT}$. This is reasonable because the contribution to the wind force according to the Bosvieux–Friedel expression [58] is weighted with the factor $x^2$.

Figure 4 shows graphs of $\delta\rho(x)/E$ versus $\hat{x}$ with $x = R_{MT}$ ($x = x \cdot \hat{x}$). Atomic units are used for $\delta\rho(x)/E$ such that 1 au $= 4\pi\varepsilon_0/a_0$, $\varepsilon_0$ being the vacuum permittivity. In figure 4(*a*) the results for two FCC systems, Ag(H) and Pd(H), with a hydrogen atom at its equilibrium position are shown. The calculations with and without the first-shell effects are labelled by 1 and 0 respectively. The electric field is in the [1 1 1] direction since only the component of the wind force in this direction is assumed to perform work. From figure 4(*a*) one notes that $\delta\rho(x)$ over the MT sphere has a dipolar character, with the dipole vector pointing in the direction of the field. Although very different in magnitude the deviation of the shape of these curves from the impurity-in-jellium result [39] is small (the Ag(H) curve was scaled with a factor 1/50). In this respect it is interesting to note that the point where $\delta\rho/E = 0$ is slightly shifted from the [$\bar{1}$1 2] direction, where it has its zero in a jellium. Besides this feature the Pd(H) curve shows a shallow maximum in the [0 0 1] direction (in the direction towards a first-shell atom). Clearly the deviations are due to the combination of the band structure of the metal and the back-scattering of the electrons by the direct environment.

In BCC metal/hydrogen systems (figure 4(*b*)) the deviations from the free-electron cosine shape are dramatic. In Nb(H) (field in the [1 0 0] direction) there is a tendency

towards a reversal of the dipole. Surely this must be the direct cause for a positive wind valence, especially when the absence of this tendency in Ta(H) is noted. The field-induced charge density at the MT radius of hydrogen in Ta shows a complex behaviour with several zeros, lacking any resemblance to the simple free-electron cosine shape. A multipolar instead of a dipolar variation of $\delta\rho(x)/E$ over the surface of the interstitial MT sphere seems to apply to the situation in Nb and Ta.

In order to give a physical interpretation of figures 4(*a*) and (*b*) one must drop the ballistic concept of electrons impinging on the impurity thereby exerting a force in the direction of the particle current. A more appropriate picture is one in which local scattering states are populated according to an incident non-equilibrium distribution of conduction electrons caused by an external field $\boldsymbol{E}$. The resulting deviation from the equilibrium charge density $\delta\rho(\boldsymbol{x})$ exerts an electrostatic force on the impurity potential. In cases where electrons are scattered over large angles, i.e. $\hat{\boldsymbol{v}}_{nk} \cdot \hat{\boldsymbol{v}}_{n'k'} < 0$, an enhanced electron density will be found at the side of the incoming particle current. At the opposite side of the scatterer a region with relative electron deficiency will exist due to a slightly lower population of incoming (Bloch) states from that side. This situation applies more or less to the case of Nb(H) as opposed to Ag(H) and Pd(H) where electron scattering is dominant in the forward direction ($\hat{\boldsymbol{v}}_{nk} \cdot \hat{\boldsymbol{v}}_{n'k'} > 0$). This results in an enhanced charge density in the forward direction with respect to the incoming field-induced particle current. Qualitatively the latter constitutes the same result as obtained from ballistic considerations.

Interestingly the concept of charge piling up against the impurity was first used by Landauer in introducing his residual resistivity dipoles (RRD) [59, 60] . The scattering Landauer implicitly had in mind corresponds to large-angle scattering, which leads to a positive contribution to the wind valence according to the explanation given above. Landauer and Woo [61] later showed that the force on an impurity due to these RRD can be of the same magnitude as the Bosvieux–Friedel (BF) part of the wind force. The RRD force is in the direction of the external field while the BF force is always in the opposite direction for an attractive electron–impurity potential. Sorbello [62] performed explicit calculations of both contributions for an s scatterer in a jellium. It turned out that the RRD field near the impurity does not necessarily have the same direction as Landauer's long-range average RRD field. In the present work the distinction between the different contributions to the wind valence is not made and no longer useful. Such a distinction has served in an early stage of the development of the theory of electromigration in order to make a second-order (RRD-like) correction to the lowest-order (BF-like) results for the charge density. Nowadays electron–impurity scattering in a metal is accounted for to all orders in the potential. This means that contributions that are first order in the electron–impurity potential and those which are of second or higher order are treated on an equal footing.

Of course the presence of the perturbed host atoms influences the electron density at the interstitial site but the ideas outlined above still apply. One aspect of large-angle scattering by the impurity can even be understood better upon inclusion of the first shell. From experiment it is known that the resistivity changes due to hydrogen in Nb and Ta are of about the same magnitude (0.65 and 0.8 $\mu\Omega$ cm/at.% respectively) but large-angle scattering by the hydrogen, as it presumably is present in Nb(H), contributes strongly. How is this reflected in the resistivity? The answer is found by performing a residual resistivity calculation for a single proton in an otherwise perfect lattice besides a calculation including charge transfer to and lattice distortion of the first shell of metal atoms. It is found [40] that in Ta $\rho_0$ increases by a factor or 7.2 upon including the first

shell (3% lattice distortion). In Nb this is only a factor of 4.7 indicating an already considerable resistivity due to the hydrogen atom alone. The $\rho_0$ values in both metals for the hydrogen alone also show that hydrogen in Nb causes a residual resistivity of 1.7 times that in Ta.

The ultimate cause of the observed difference in the field-induced charge density at the hydrogen in Nb and in Ta must be found in the electronic structure of the atoms composing the host metal. From figures 2(*d*) and (*e*) the differences in reciprocal space are seen to be not significant. Although $Z = 73$ for Ta the relativistic effects on the shape of the Fermi surface (lifting of degeneracies due to $LS$ coupling) are known to be small [63]. In the free atom the charge densities are likely to be influenced by the so-called relativistic s contraction of even the valence 6s shell in Ta. For Sm ($Z = 62$) Pyykkö [64] reports a relativistic s contraction of the $6s_{1/2}$ orbital of about 5%. For Pu ($Z = 94$) this is already 14% for the $7s_{1/2}$ shell.

Another striking difference between the two metals, namely the completely filled 4f shell in Ta, enhances this effect. In general f electrons do not screen the nuclear charge very efficiently leading to a greater effective nuclear charge as seen by the outermost valence electrons. In for instance the lanthanide series this leads to the so-called lanthanide contraction [65]: a decrease in the size of the 3+ lanthanide ions and an increase in the oxidation potential ($M \rightarrow M^{3+}$) along the series.

The chemistry of heavier transition metals is also affected by the lanthanide contraction and the relativistic s contraction. For Au the combination of these two effects explains the existence of an $Au^-$ auride ions in CsAu while no such compounds are known for Ag [64].

From the output of the relativistic atomic SCF program it is indeed found that the outermost s electrons in Nb are on average about 0.5 Bohr further away from the nucleus than in Ta (3.806 Bohr versus 3.278 Bohr respectively). The average value of $r$ for the d electrons is somewhat larger for Ta (2.017 Bohr) than for Nb (1.992 Bohr), the increase however being much smaller than when going from V (1.283 Bohr) to Nb.

Evidently nature offers room for considerable differences between the spatial distribution of charge in the metals Nb and Ta. To some extent crystal potentials constructed from relativistic atomic charge densities retain the atomic contraction effects. Consequently the scattering of Bloch electrons by an interstitial hydrogen atom will be influenced although the precise mechanism causing the difference in wind valence between Nb and Ta is not yet understood.

### *4.4. Hydrogen/deuterium isotope effect*

Utilizing a simple zero-point motion model for the hydrogen atoms moving in a harmonic potential well in all cases, except for H and D in Al and Ni, a significant isotope effect was noticed. The reason for the application of the zero-point motion model is that the actual oscillatory motion of the hydrogen isotope is not affected seriously by the electric field. This was already shown in calculating the displacement of the isotope from its equilibrium position in section 3.1. An alternative illustration is offered by comparing the maximum change in charge density at $E = 100\ \mathrm{V\ m^{-1}}$ in Ag(H) with the average charge density in Ag. The resulting ratio $\delta\rho/\rho \simeq 10^{-9}$ again shows that electromigration will be noticed only in macroscopic ensembles of hydrogen isotopes exposed to an electric field over a very long period of time (1 day $\simeq 1.79 \times 10^{21}$ atomic units of time).

Assuming a constant value for the direct valence a remarkable qualitative agreement between theoretical and experimental ratios $Z^*_H/Z^*_D$ emerges. This ratio turns out to be

smaller than unity in Ag and V but larger in Pd, Nb and Ta, in agreement with experiment. In addition, both a larger wind valence for the proton than for the deuteron as well as the opposite situation emerge in a natural way. The proton/deuteron probability density weighting a decreasing wind valence curve (like in V) results in $Z^{H}_{wind} < Z^{D}_{wind}$ while an increasing curve (like in Nb) leads to $Z^{H}_{wind} > Z^{D}_{wind}$. Previous explanations have only been successful in either the first [8, 66] or the second [67] situation.

### *4.5. Temperature effects*

In I possible contributions due to inelastic inter-band transitions were discussed and claimed to be relatively unimportant. The importance of intra-band contributions at non-zero temperatures, also described in I, can be estimated by performing wind valence calculations at energies $\varepsilon_F + kT$ and $\varepsilon_F - kT$ in addition to $\varepsilon = \varepsilon_F$. The energy integral in equation (67) of I can now be roughly approximated by a weighted average of the obtained wind valences at the three energies.

It is expected that such temperature effects will be most pronounced in situations where the DOS around $\varepsilon_F$ varies rapidly. Pd and Nb provide two examples of such behaviour. The experiments on Pd(H) were carried out at $kT \simeq 6$ mRyd while for Nb(H) $kT \simeq 3$ mRyd.

Application of the computational scheme to a hydrogen atom in Nb at its equilibrium position (3% lattice distortion) at energies 0.849, 0.852 and 0.855 Ryd resulted in wind valences 2.34, 1.68 and 0.68 respectively. By itself the variation of $Z_{wind}(0)$ with energy can be called considerable. The DOS at these energies (6.53, 6.25 and 5.88 $Ryd^{-1}$ respectively) also varies considerably, indicating that the energy interval under consideration is situated on the right-hand side of the narrow peak in the DOS of Nb [29]. After taking the average of these figures with the energy derivative of the Fermi–Dirac distribution as the weight function ($(1 - f_0)f_0 = 0.197$ at $\varepsilon = \varepsilon_F \pm kT$ and 0.25 at $\varepsilon = \varepsilon_F$), the final result is $Z_{wind}(0) = 1.58$, deviating 6.0% from the value at $\varepsilon_F$. For hydrogen in Pd a similar behaviour is found.

Obviously the influence of thermal broadening of $\partial f_0(\varepsilon)/\partial\varepsilon$ on the wind valence remains small when the energies above and below $\varepsilon_F$ cover a region where the DOS varies more or less linearly. This surely is the case for Cu and Ag (nearly constant DOS) and at moderate $kT$ for Nb and Pd. At much higher temperatures more care has to be taken and perhaps a weighted average over wind valences at different energies is essential for obtaining agreement with experimental data. Examples are constituted by the Nb(C) and Nb(O) systems, which have been investigated experimentally at about 2500 K ($kT \simeq$ 16 mRyd). Also most data on the electromigration of substitutional impurities in Nb and other metals have been obtained at such high temperatures. A look at the DOS of Nb immediately reveals that in this case the whole peak around the Fermi energy will contribute.

## 5. Conclusions

In this work results of the calculation of the electromigration wind valence using the KKR Green function method were presented. Lattice distortion and charge-transfer effects

were accounted for properly and the angular momentum cut-off was taken at $l = 3$. The following summarizing remarks can be made:

(i) The generally non-scalar, position-dependent wind valence could be successfully reduced to a scalar upon taking into account the microscopic degrees of freedom leading to diffusion of the oscillating interstitial. For V(H), Nb(H) and Ta(H) this procedure yielded the right sign of $Z_{\text{wind}}$ only when adopting a curved migration path instead of the straight path in the [1 1 0] direction. Thus this critical dependence of the sign of the wind valence on the adopted migration path provided further insight into the elementary diffusion step of hydrogen in BCC metals.

(ii) The position-dependent wind valences were averaged along the migration path, weighted by a function describing the probability of finding the impurity along the path. The value of this procedure is most clearly illustrated by the Pd(H) system. Simple averaging (i.e. a constant weight function) leads to $Z_{\text{wind}} = -0.23$, averaging with a harmonic oscillator weight function gives $Z_{\text{wind}} = -0.43$, while the value at the equilibrium position is $Z_{\text{wind}} = -0.75$. The middle value is most compatible with a direct valence somewhat smaller than unity as deduced from the proton Hall effect in Pd(H) and from the measured $Z^* = 0.44$. In addition the probability density introduces the possibility of accounting for a difference in zero-point motion between H and D. Assuming the direct valence to be the same for H and D, for the first time a qualitative agreement was obtained for the ratios $Z^*_H/Z^*_D$ when compared with experimental ratios, except for Ni(H/D).

(iii) regarding the experimentally observed difference in sign of the wind valence of H in Nb (positive) and in Ta (negative), it can be stated that this is due to different field-induced charge densities at the impurity site. The Nb Bloch electrons on the third-zone part of the Fermi surface (the jungle gym sheet) are scattered in such a way by the impurity that a charge distribution is built up with an almost reversed dipole moment when compared to H in Ag, Pd and in a free-electron gas. In tantalum the field-induced charge density also deviates strongly from the FCC metal/impurity results but still with an electric dipole moment in the direction of the external field. Presumably the difference between Nb and Ta is due to the high atomic number of Ta. The resulting relativistic effects lead to differences in the atomic charge distribution and therefore in the crystal potential.

(iv) Compared with experiment the quality of the results presented in this work in general is very satisfactory although there exists a dependence on the calculated transport relaxation time, the potentials used and the way in which temperature effects are incorporated.

As far as the transport relaxation time is concerned it is noticed that $\tau$ as obtained via the explicit Fermi surface integration substantially improves the results with respect to free-electron transport relaxation times. These $\tau$ values, satisfying their purpose so well, stem from a KKR calculation with largest possible MT radii. Especially for the BCC metals large differences emerge upon decreasing the MT radius. Although completely isotropic the use of such $\tau$ values is apparently justified a posteriori in view of the success for a wide variety of metal/hydrogen systems. Of course part of the anisotropy of the vector mean free path was retained through the velocity field over the Fermi surface.

The potentials have been constructed by an approved method. Via a deliberate shift procedure charge neutrality was guaranteed. In this shift procedure the number of degrees of freedom was less than or equal to 2. Independent variation of these degrees of freedom influenced the wind valences along the path to some extent but only in

regions where the impurity probability density is low. The final results were not affected significantly. Inclusion of the first shell (at experimental or estimated lattice distortion) leads to a different multiple scattering and thus to a change in the wavefunction. The influence on $Z_{wind}$ varied for the different systems but was never found to be as spectacular as is seen in the calculation of the residual resistivity [40] and the de Haas–van Alphen scattering quantities [32].

The temperature dependence of the wind valence at moderate temperatures at which metal/hydrogen systems are studied experimentally is due to variation in $\tau$. At higher temperatures, close to the melting point of the metal, elastic scattering at energies several $kT$ above and below the Fermi energy contributes. Depending on the shape of the DOS curve around the Fermi energy the energy dependence of the wind valence can be considerable. Such effects are expected to be important for the electromigration of substitutional impurities in Nb and might explain the change of sign in $Z^*$ of O in Nb at 2100 K.

(v) In the discussion concerning the value of the direct valence the conclusion to be drawn from the present work must be that (apart from Cu(H) and Ag(H) where the wind valence strongly dominates the direct valence) the scalar direct valence is definitely different from zero but smaller than unity in real metals. Just like the wind valence the direct valence will have a tensorial character and should be reduced to a scalar in a similar way as the wind valence. The direct valence must be viewed as resulting from the interaction between the charge density at the interstitial site, the impurity nucleus and the electric field. Tightly bound core states are able to follow the impurity motion adiabatically. Even the very rapidly accelerated motion of the nucleus is instantaneously followed by the electrons in (polarized) bound states. In such a situation an electric field cannot exert a force on the impurity. An isolated hydrogen atom does not gain momentum under the influence of an electric field [68]. Complete vanishing of the contribution to the direct force from that part of the nuclear charge corresponding to electrons in core states was already noticed in several theoretical papers on electromigration [69, 70]. If however the (non-spherically symmetric) electron cloud around the impurity in a metal is unable to follow the nucleus quickly in its motion, total cancellation of all forces need no longer be guaranteed, providing room for a direct force.

Apart from a possible failure of the Born–Oppenheimer approximation for electrons in valence states (especially Rydberg states in highly excited atoms and molecules), newly introduced charge might become more or less immobilized on the surrounding metal atoms and will not be entirely available in the delicate process of dynamic screening. In addition, concentrating on hydrogen as an impurity, the bound state for the electron is replaced by a scattering state in the metal and is counted in the Friedel sum. An electron in such a scattering state is less susceptible to the motion of the proton, indicating a possible breakdown of the Born–Oppenheimer approximation. In this sense a vanishing direct valence would imply justification of the Born–Oppenheimer approximation in the screening problem. If this assertion is true, a theoretical treatment of the proton screening problem, where it is assumed that the electrons follow the impurity adiabatically, should lead to a vanishing direct force [71].

## References

[1] Feenstra R, Brouwer R and Griessen R 1988 *Europhys. Lett.* 7 425

[2] Verbruggen A H, Griessen R and de Groot D G 1986 *J. Phys. F: Met. Phys.* **16** 557
[3] Wipf H 1978 *Topics in Applied Physics* vol 29 *Hydrogen in Metals II* (Berlin: Springer)
[4] Brouwer R and Griessen R 1989 *Phys. Rev. Lett.* **62** 1760
[5] de Groot S R 1942 *Physica* **9** 699
[6] van Ek J and Lodder A 1991 *J. Phys.: Condens. Matter* **3** 7307
[7] Eichenauer W, Loser W and Witte H 1965 *Z. Metallkd.* **56** 287
[8] Einziger R E and Huntington H B 1974 *J. Phys. Chem. Solids* **35** 1563
[9] Wipf H and Erckmann V 1976 *Scr. Metall.* **10** 813
[10] Hérold A 1956 *C. R. Acad. Sci. Paris* **243** 806
[11] Marêché J-F, Rat J-C and Hérold A 1975 *C.R. Acad. Sci. Paris* **281** 449
[12] Erckmann V and Wipf H 1976 *Phys. Rev. Lett.* **37** 341
[13] Pine D J and Cotts R M 1983 *Phys. Rev.* B **28** 641
[14] Nakajima H, Yoshioka M and Koiwa M 1987 *Acta Metall.* **35** 2731
[15] Schmidt F A and Warner J C 1967 *J. Less-Common Met.* **13** 493
[16] Schmidt F A and Carlson O N 1972 *J. Less-Common Met.* **26** 247
[17] Fromm E, Kirchheim R and Mathuni J 1975 *J. Less-Common Met.* **43** 211
[18] Kirchheim R and Fromm E 1974 *Acta Metall.* **22** 1397
[19] Ashcroft N W and Mermin N D 1981 *Solid State Physics* (Tokyo: Holt-Saunders)
[20] Eichenauer W 1968 *Z. Metallkd.* **59** 613
[21] Karlsson E B 1989 *Int. J. Quantum Chem.* **35** 779
Sugimoto H and Fukai Y 1980 *Phys. Rev.* B **22** 670
[22] Portis A and Crowe K M 1986 *Phys. Lett.* A **117** 234
[23] Puska M J and Nieminen R M 1984 *Phys. Rev.* B **29** 5382
[24] Kehr K W 1978 *Topics in Applied Physics* vol 29 *Hydrogen in Metals I* (Berlin: Springer)
[25] Richter D 1979 *Hyperfine Interactions* **6** 193
[26] Oppeneer P M and Lodder A 1988 *J. Phys. F: Met. Phys.* **18** 869
[27] Wipf H 1976 *J. Less-Common Met.* **49** 291
[28] Oppeneer P M, Lodder A and Griessen R 1988 *J. Phys. F: Met. Phys.* **18** 1733
[29] Moruzzi V L, Janak J F and Williams A R 1978 *Calculated Electronic Properties of Metals* (Oxford: Pergamon)
[30] Matheiss L F 1964 *Phys. Rev.* **134** 970
[31] Desclaux J P, Moser C M and Verhaegen G 1971 *J. Phys. B: At. Mol. Phys.* **4** 296
[32] Oppeneer P M and Lodder A 1987 *J. Phys. F: Met. Phys.* **17** 1901
[33] Lehmann G 1975 *Phys. Status Solidi* b **70** 737
[34] Lasseter R H and Soven P 1973 *Phys. Rev.* B **8** 2476
[35] Molenaar J, Lodder A and Coleridge P T 1983 *J. Phys. F: Met. Phys.* **13** 839
[36] *Landolt–Börnstein New Series* 1982 vol 15a (Berlin: Springer)
[37] Coleridge P T 1972 *J. Phys. F: Met. Phys.* **2** 1016
[38] Mertig I, Mrosan E and Ziesche P 1987 *Multiple Scattering Theory of Point Defects in Metals: Electronic Properties* (Leipzig: Teubner)
[39] Lodder A 1984 *J. Phys. F: Met. Phys.* **14** 2943
[40] van Ek J and Lodder A 1991 *J. Phys: Condens. Matter* at press
[41] Seeger A 1978 *Topics in Applied Physics* vol 29 *Hydrogen in Metals I* (Berlin: Springer)
[42] Cotts R M 1978 *Topics in Applied Physics* vol 29 *Hydrogen in Metals I* (Berlin: Springer)
[43] Sköld K 1978 *Topics in Applied Physics* vol 29 *Hydrogen in Metals I* (Berlin: Springer)
[44] van Ek J and Lodder A 1990 *Solid State Commun.* **73** 373
[45] Springer T 1978 *Topics in Applied Physics* vol 29 *Hydrogen in Metals I* (Berlin: Springer)
[46] Völkl J and Alefeld G 1974 *Diffusion in Solids: Recent Developments* (New York: Academic)
[47] Wagner F E and Wortmann G 1978 *Topics in Applied Physics* vol 29 *Hydrogen in Metals I* (Berlin: Springer)
[48] Suzuki T 1985 *Trans. Inst. Met.* **26** 601
[49] Brouwer R, Douwes H, Griessen R and Walker E 1987 *Phys. Rev. Lett.* **58** 2551
[50] Behr H, Keppler H M, Streyer G, Metzger H and Peisl J 1983 *J. Phys. F: Met. Phys.* **13** L29
[51] Sidorenko V M, Kripyakevich R I and Kachmar B F 1969 *Fiz. Khim. Mekhan. Mat.* **5** 187
[52] Teichler H 1979 *Z. Phys. Chem. NF* **114** 155
[53] Fiks V B 1959 *Sov. Phys.–Solid State* **1** 14
[54] Huntington H B and Grone A R 1961 *J. Phys. Chem. Solids* **20** 76
[55] Verbruggen A H, Griessen R and Rector J H 1984 *Phys. Rev. Lett.* **52** 1625

[56] Lodder A 1991 *J. Phys.: Condens. Matter* **3** 399
[57] Sorbello R S 1973 *J. Phys. Chem. Solids* **34** 937
[58] Bosvieux C and Friedel J 1962 *J. Phys. Chem. Solids* **23** 123
[59] Landauer R 1957 *IBM J. Res. Dev.* **1** 223
[60] Landauer R 1975 *Z. Phys.* B **21** 247
[61] Landauer R and Woo J W F 1974 *Phys. Rev.* B **10** 1266
[62] Sorbello R S 1981 *Phys. Rev.* B **23** 5119
[63] Cracknell A P and Wong K C 1973 *The Fermi Surface* (Oxford: Clarendon)
[64] Pyykkö P 1978 *Advances in Quantum Chemistry* vol II (New York: Academic)
[65] Mackay K M and Mackay R A 1981 *Introduction to Modern Inorganic Chemistry* 3rd edn (London: International Textbook Company)
[66] Lodder A and Brand M G E 1984 *J. Phys. F: Met. Phys.* **14** 2955
[67] Stoneham A M and Flynn C P 1973 *J. Phys. F: Met. Phys.* **3** 505
[68] Sorbello R S and Dasgupta B B 1980 *Phys. Rev.* B **21** 2196
[69] Schaich W L 1976 *Phys. Rev.* B **13** 3350
[70] Rimbey P R and Sorbello R S 1980 *Phys. Rev.* B **21** 2150
[71] Lodder A 1989 *Physica* A **158** 723